OPEN

Correspondence and
requests for materials
should be addressed to
X.Y.H. (xiaoyonghu@
pku.edu.cn) or Q.H.G.
(qhgong@pku.edu.cn)

Chip-integrated ultrawide-band all-optical logic comparator in plasmonic circuits

Cuicui Lu[1], Xiaoyong Hu[1,2], Hong Yang[1] & Qihuang Gong[1,2]

[1]State Key Laboratory for Mesoscopic Physics & Department of Physics, Peking University, Beijing 100871, People's Republic of China, [2]Collaborative Innovation Center of Quantum Matter, Beijing 100871, People's Republic of China.

Optical computing opens up the possibility for the realization of ultrahigh-speed and ultrawide-band information processing. Integrated all-optical logic comparator is one of the indispensable core components of optical computing systems. Unfortunately, up to now, no any nanoscale all-optical logic comparator suitable for on-chip integration applications has been realized experimentally. Here, we report a subtle and effective technical solution to circumvent the obstacles of inherent Ohmic losses of metal and limited propagation length of SPPs. A nanoscale all-optical logic comparator suitable for on-chip integration applications is realized in plasmonic circuits directly. The incident single-bit (or dual-bit) logic signals can be compared and the comparison results are endowed with different logic encodings. An ultrabroad operating wavelength range from 700 to 1000 nm, and an ultrahigh output logic-state contrast-ratio of more than 25 dB are realized experimentally. No high power requirement is needed. Though nanoscale SPP light source and the logic comparator device are integrated into the same plasmonic chip, an ultrasmall feature size is maintained. This work not only paves a way for the realization of complex logic device such as adders and multiplier, but also opens up the possibility for realizing quantum solid chips based on plasmonic circuits.

P hotons can be used as information carriers, making it possible to reach ultrahigh-speed and ultrawide-band information processing based on optical computing, which is a long-term pursuit of researchers. Researchers dream of achieving a photonic computer with untiring efforts. A crucial point is to realize the photon center processing unit (CPU) which is mainly composed of all-optical logic devices. Several schemes have been proposed in the past years, such as using photonic crystals[1], silicon photonics[2], surface plasmon polaritons (SPPs)[3,4]. The lattice constant of photonic crystal is in the scale of light wavelength, so it is difficult to fabricate ultrasmall all-optical logic devices based on photonic crystals. Silicon photonics generally needs the help of electric voltage and depends on the mature CMOS technology; it is also difficult to realize pure all-optical integrated logic devices based on silicon. SPPs, a kind of electromagnetic mode coupled to the oscillations of conduction electrons that propagate along the interface between metal and dielectric materials, have been regarded as a promising candidate to further miniaturize all-optical devices due to its tremendous subwavelength field confinement properties[5,6]. However, to date, small experimental progress has been made in nanoscale all-optical logic devices based on SPPs, and there is not any experimental report in nanoscale all-optical complex logic devices based on SPPs[7–11]. Part of the reason lies in the enormous Ohmic losses of metal in the visible and near-infrared range. All-optical logic comparator devices are indispensible and core components of optical computing systems. Traditionally, semiconductor optical amplifiers are adopted to realize all-optical logic comparator devices[12–14]. The high operating threshold intensity of GW/cm² and large size of hundreds of micrometers seriously restrict the practical on-chip integration application of logic comparator devices[15–17]. Up to now, no feasible realization method for integrated all-optical logic comparator has been proposed, and no any nanoscale all-optical logic comparator suitable for on-chip integration applications has been realized experimentally. This forms an enormous obstacle to the realization of optical computing systems.

Here, we report a subtle and effective technical solution to realize nanoscale integrated all-optical logic comparator suitable for practical on-chip applications in plasmonic circuits directly. A tapered nanoslit array connected with a plasmonic crystal in the left-hand side is used as the on-chip SPP light source. A single nanoslit converts a part of the incident light energy to SPPs[18]. The tapered nanoslit array effectively enhances the SPP intensity because more incident light signals are converted into SPPs. The distance between the first nanogroove

of the plasmonic crystal and the first nanoslit is equal to the lattice constant of the plasmonic crystal, which forms a wideband unidirectional SPP light source, i.e., the left-going SPPs are forbidden, and there only exist right-going SPPs in the interface of metal and dielectric cover layer. The remaining part of the incident light signals is scattered by the tapered nanoslit array, which corresponds to the input logic signal of "1". While no scattered light, implying no incident light signal, corresponds to the input logic signal of "0". The logic comparison function is realized based on the high digit priority principle, i.e. the high digit determines the output logic state. In our experiment, we adopt a straight dielectric-loaded plasmonic waveguide and a dielectric-loaded plasmonic waveguide having Mach-Zehnder interferometer configuration etched in a gold film coated with an organic polymer layer to perform the logic comparison operation. The incident single-bit (or dual-bit) logic signals can be compared and the comparison results are endowed with different logic encodings. The SPP propagation length in the polymer-loaded plasmonic waveguide used in our experiment is about two times to the traditional plasmonic slot waveguides and silver nanowires[19,20]. Moreover, the polymer-loaded plasmonic waveguide used in our experiment provides tremendous field confinement, and accordingly ensures a violent modulation of the SPP propagation by using an ultrasmall plasmonic microstructure. The obstacles of strong Ohmic losses of metal and limited propagation length of SPPs are circumvented. An ultrabroad operating wavelength range from 700 to 1000 nm, an ultrahigh output logic state contrast ratio of more than 25 dB, and excellent single-bit (and dual-bit) logic comparison function are realized experimentally in plasmonic circuits directly. Though the logic comparator device and the ultrabroad band unidirectional SPP source is integrated into the same plasmonic chip, the lateral dimensional is less than 10 μm for single-bit logic comparator, and less than 20 μm for dual-bit logic comparator. Moreover, no high power requirement is needed. This work not only paves a way for the realization of complex logic device such as adders and multiplier, but also opens up the possibility for realizing quantum solid chips based on plasmonic circuits.

Results

Characteristic of the proposed plasmonic waveguide. The three-dimensional schematic structure of the dielectric-loaded plasmonic straight waveguide is shown in Fig. 1a. The gold film with a thickness of 300 nm is coated with a 250-nm-thick organic polymer layer made of polyvinyl alcohol (PVA) on silicon dioxide substrate. The input port is composed of a tapered nanoslit array connected with a one-dimensional (1D) plasmonic crystal on the left-hand side. The plasmonic crystal has five air nanogrooves with a depth of 350 nm, width of 200 nm, and length of 6 μm. The lattice period of the plasmonic crystal is 320 nm. The distance between the first nanoslit and the first air nanogroove of the plasmonic crystal is equal to the value of the lattice constant. The depth and width of the nanoslits are 550 and 250 nm, respectively. The length of the nanoslits was 6 μm for the first one, 4.4 μm for the second one, 3.6 μm for the third one, 2.8 μm for the fourth one, and 2 μm for the last one. The width and height of the PVA waveguide were 400 nm and 250 nm, respectively, which ensures single SPP mode propagation with the Y-direction polarization when the wavelength of the incident light was more than 850 nm. The exit port is constructed by decoupling grating composed of four grooves with width of 250 nm, depth of 300 nm, length of 4.4 μm and period of 500 nm, in order to convert SPPs into scattered light for the purpose of measurement, as shown in Fig. 1b. Though SPPs can be excited efficiently by a signal light incident from the top (or bottom)[18], in our experiment, we used a signal light incident from the bottom of the sample to facilitate the experimental measurements. To study the influences of the 250-nm-thick PVA layer on the propagation properties of SPP modes, we calculated the dispersion curve of the
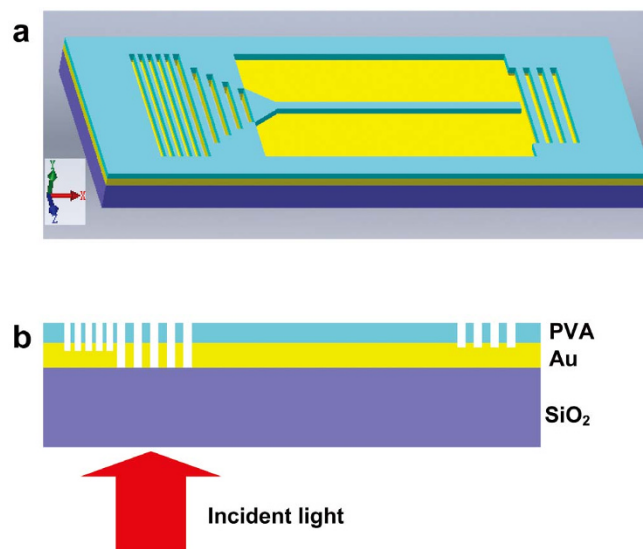

Figure 1 | Schematic diagrams of the plasmonic waveguide. (a) Three-dimensional model for the plasmonic waveguide with excitation port and output decoupling grating. (b) Cross-section schematic structure.

SPP mode as a function of incident light wavelength in a 300-nm-thick gold film coated with a 250-nm-thick PVA layer by using the finite element method (adopting a commercial software package COMSOL Multiphysics)[11], and the calculated results are shown in Fig. 2a. The wavelength-dependent complex dielectric function of gold was obtained from Ref. 21. The refractive index of PVA was 1.5 in the visible and near infrared range[22]. Even SPPs at short wavelength can still propagate a couple of microns until their intensity is smaller by factor 1/e, as shown in Fig. 2a. To further make clear the role of the 250-nm-thick PVA layer, we calculated the magnetic-field distribution of a 850-nm incident light signal in the plane of 125 nm above the gold film for two structures, i.e., 300-nm-thick gold film in air (Au-air structure) and 300-nm-thick gold film coated with a 250-nm-thick PVA layer in air (Au-PVA-air structure), by using the finite element method, and the calculated results are shown in Fig. 2b. There was a small magnetic-field distribution for the SPP mode in this plane for the Au-air structure, but the distribution was different for the Au-PVA-air structure, i.e., the structure used in our experiment. There was strong magnetic-field distribution associated with the SPP mode in the PVA layer, which implies that a very tight field confinement is formed in the Au-PVA-air structure. This is further confirmed by our calculated power flow distribution (Fig. 2c) in the Y direction for the SPP mode, with an origin at the bottom of gold film and 1000 nm away from the nanoslit, for the Au-air and Au-PVA-air structures. About 80% of the power flow was confined in the PVA layer for the Au-PVA-air structure. Thus a much stronger modulation of the SPP propagation is produced despite only several nanogrooves being etched in the Au-PVA-air structure compared with that in the Au-air structure. Thus, an ultrasmall feature size of the all-optical logic device can be anticipated. Barnes *et al.* have pointed out that a 1D plasmonic crystal can produce a SPP stop band if the lattice period is nearly half the SPP wavelength[23]. Thus, the sinistral plasmonic crystal acts as a perfect Bragg reflector. The air nanogroove depth of the sinistral plasmonic crystal is 350 nm, indicating that the air nanogrooves are etched through the PVA layer and also etched into the gold film. Because of the deeply etched air nanogrooves, the Au-PVA-air structure modulated SPP propagation enormously. The left-going SPPs for which their wavelengths fall within the stop band of the sinistral plasmonic crystal are reflected completely, and then propagate towards the right direction. To study the unidirectional SPP launching properties, we calculated the transmittance spectrum
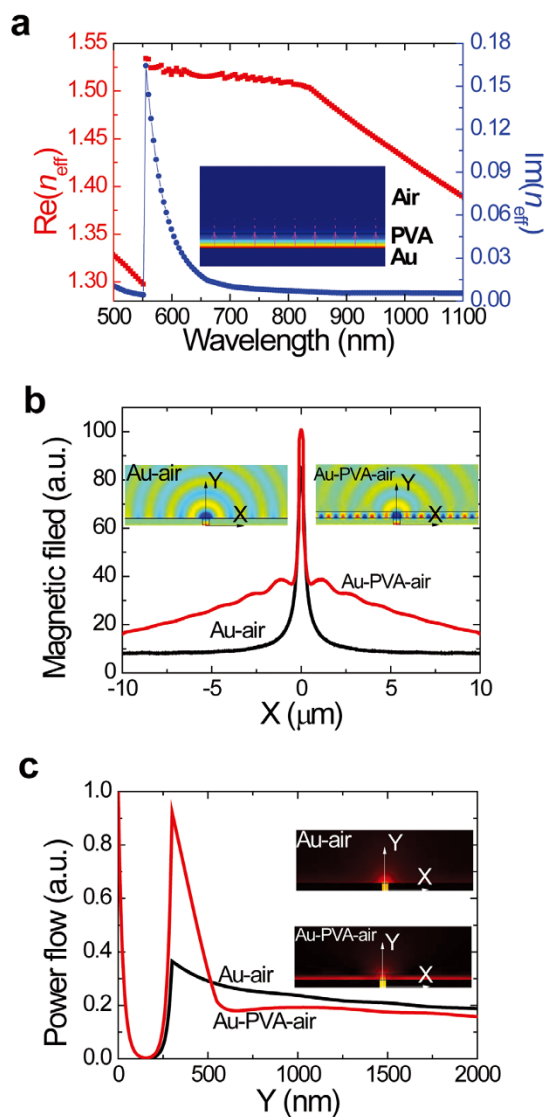
Figure 2 | Characteristics of the Au-PVA configuration. (a) Dispersion curve for 300-nm thick film coated with 250-nm thick PVA polymer layer. Re(n_{eff}) and Im(n_{eff}) denote the real part and imaginative parts of the SPP effective refractive index, respectively. Insert shows the SPP at the interface of Au and PVA. The pink arrows indicate the electric field direction of SPPs. (b) Calculated magnetic field distribution in a plane of 125 nm above the gold film for an 850-nm incident light in the Au-air and Au-PVA-air structures. Inserts show calculated magnetic field distribution in the cross section of Au-air and Au-PVA-air structures, where the nanoslit has a depth of 550 nm and width of 250 nm. (c) Calculated power flow distribution in the Y direction 1000 nm away from the nanoslit center for an 850-nm incident light in the Au-air and Au-PVA-air structures. Inserts show calculated power flow distribution in the cross section of Au-air and Au-PVA-air structures.

of the 1D plasmonic crystal by using the finite element method, and the calculated result is shown in Fig. 3a. It is clear that there is an ultrawide-band SPP stop band from 690 nm to 1150 nm, covering a wavelength range of 460 nm. We also calculated the extinction ratio of the steady-state power flow for right side of the nanoslit array to the left side of the plasmonic crystal, which is shown in Fig. 3b. The average extinction ratio is about 25 dB for the ultra-wide stop band, which among the highest values compared with the previous reports[24,25]. To further confirm the unidirectional SPP launching properties and give clear presentations, we calculated the magnetic field distribution of *Hz* component (Fig. 3c, 3d, 3e, 3f) and power

flow distribution (Fig. 3g, 3h, 3i, and 3j) from 690 nm to 1150 nm at the cross-section of the SPP launcher. It is obvious that the left-going SPPs were reflected completely and subsequently propagated in the right direction. This is further confirmed by our recent measurements[11,26]. Unidirectional SPP launching is attained in a very wide wavelength range from 690 to 1150 nm. The operating bandwidth, 460 nm, is enlarged by two orders of magnitude compared with those previously reported[24,25]. To investigate the propagation properties single SPP waveguide mode, we calculated its propagation length of the dielectric loaded waveguide, which is shown in Fig. 4a. When the incident wavelength is more than 850 nm, the propagation length is more than 11.3 μm. Fig. 4b shows the top-view scanning-electron-microscope (SEM) image of a straight plasmonic waveguide sample, fabricated by the focused-ion-beam (FIB) etching system. The length of the straight waveguide is 15 μm. To confirm the propagation properties of the plasmonic waveguide with highly-efficient excitation, a micro-spectroscopy measurement system is adopted to measure the light intensity of the sample. An obvious bright spot can be observed at the exit port of the straight waveguide with 850-nm incident wavelength. To further confirm the propagation properties of the SPP mode in the plasmonic waveguide, we also etched a 90° circular arc waveguide with a radius of 1000 nm at the upper part and 1600 nm at the lower part, as shown in Fig. 4d. The whole length of the bend plasmonic waveguide is 11.6 μm. Fig. 4e shows the dark field CCD image of the bend waveguide under excitation of a continuous wave (CW) incident laser with a wavelength of 850 nm measured by the micro-spectroscopy measurement system. Also a distinctive output signal can be observed at the exit port of the bend waveguide thought the loss is serious at the corner, which also proves our excitation method of tapered slits jointed to plasmonic crystal is very efficient.

Single-bit all-optical logic comparator. Figure 5a illustrates the function of all-optical logic comparator for the single-bit logic signals. When the incident logic signals '1' is inputted in the port '+' while '0' in the port '-', an output logic state of '1' is obtained, which implies that the logic signal in the port '+' is larger than that in the port '-'. When the incident logic signals '0' is inputted in the port '+' while '1' in the port '-', an output logic state of '0' is obtained, which implies that the logic signal in the port '+' is less than that in the port '-'. The SEM image of the logic comparator sample performing the logic operating of single bit logic signal comparison is shown in Fig. 5b and g, which is composed of a straight PVA-loaded plasmonic waveguide and a PVA-loaded plasmonic waveguide connected with a Mach-Zehnder interferometer. There was a certain optical path difference of 394 nm between two arms of the Mach-Zehnder interferometer, which results in a destructive interference for the SPPs generated by the incident light with a wavelength of 985 nm in the output waveguide. To perform the logic operation of comparison between logic signals '1' and '0', we etched a SPP light source, i.e., a tapered nanoslit array having a plasmonic crystal in the left-hand side, connected with a triangular access waveguide only in the input port of the straight plasmonic waveguide, as shown in Fig. 5b. Under excitation of a 700-nm CW incident light, there was strong scattered light only in the input port of the straight plasmonic waveguide, which indicates that the logic signal '1' is inputted into the straight plasmonic waveguide, while the logic signal '0' is inputted in the plasmonic waveguide connected with a Mach-Zehnder interferometer. Remarkable scattered light was obtained from the decoupling grating in output port, as shown in Fig. 5c, which corresponds to the output logic '1'. This implies that the logic signal propagated in the straight plasmonic waveguide is larger than that in the plasmonic waveguide connected with a Mach-Zehnder interferometer. The same case was obtained when the logic comparison sample was excited by a CW incident light with a wavelength of 800 nm (Fig. 5d), 900 nm (Fig. 5e), and 1000 nm
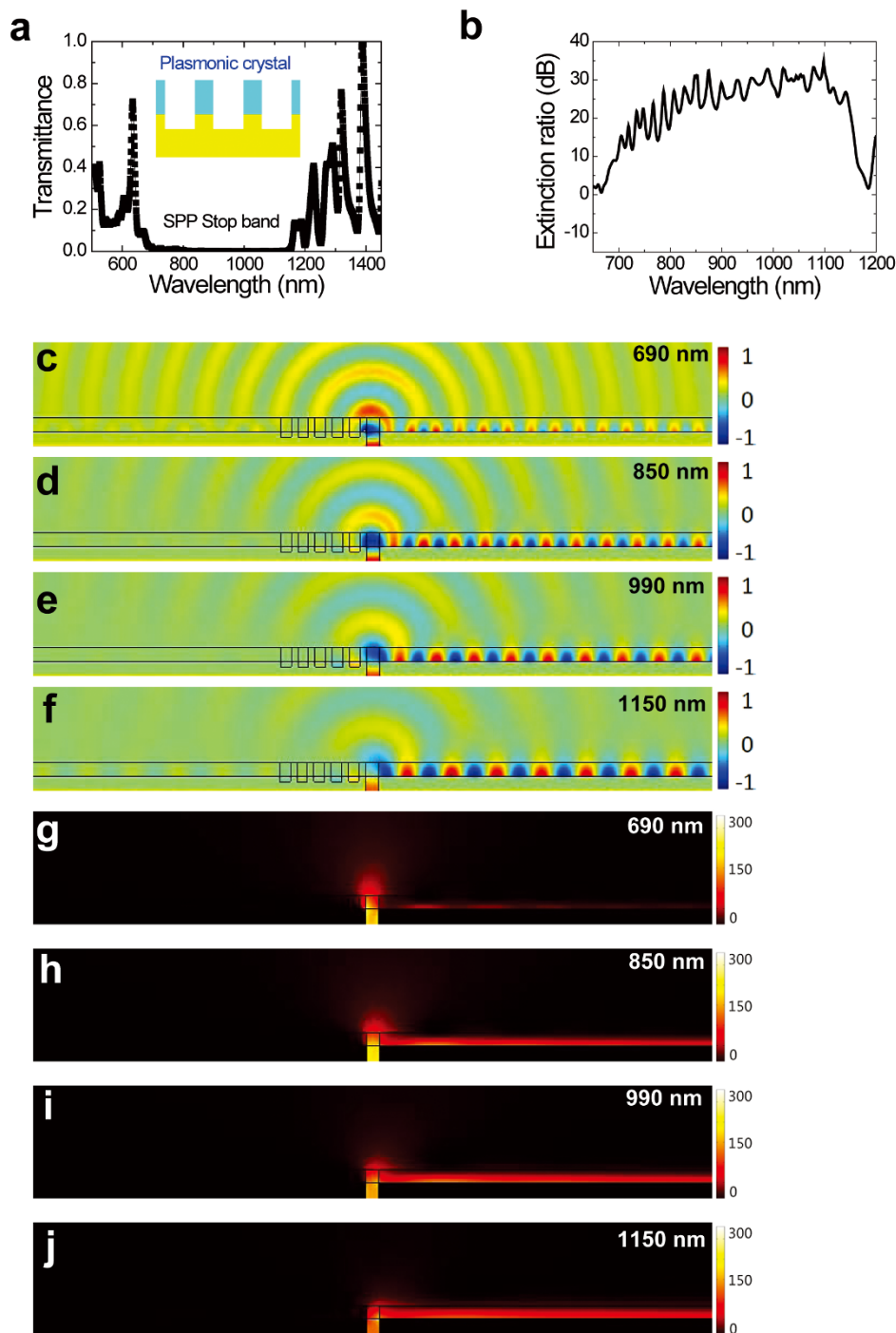
3

Figure 3 | Characteristics of the broadband unidirectional SPP launchers. (a) Calculated transmission spectrum of the 1D plasmonic crystal. Insert shows the cross-section of the 1D plasmonic crystal where the yellow color denotes Au and the green color denotes polymer PVA. (b) Calculated extinction ratio of the steady-state power flow for right side of the nano-slit to the left side of the plasmonic crystal. Calculated steady-state field distribution of Hz component in the cross section of the 1D plasmonic crystal under excitation of an incident light with a wavelength of 690 nm (c), 850 nm (d), 990 nm (e) and 1150 nm (f). Calculated steady-state power flow distribution in the cross section of the 1D plasmonic crystal under excitation of an incident light with wavelength of 690 nm (g), 850 nm (h), 990 nm (i) and 1150 nm (j).

(Fig. 5f). The measured results are in agreement with the calculated ones by using the finite element method shown in Fig. S1 in the Supplementary Information. This indicates that the logic comparison sample performs excellently in a large wavelength of 300 nm. The excellent propagation of SPPs in the PVA-loaded plasmonic waveguide ensures perfect logic comparison operation. The weak logic state of "1" in Fig. 5(d) originates from a weak intensity of the incident 800-nm CW laser beam. To perform the

logic operation of comparison between logic signals '0' and '1', we etched a SPP light source connected with a triangular access waveguide only in the input port of the plasmonic waveguide connected with a Mach-Zehnder interferometer, as shown in Fig. 5f. Under excitation of a 700-nm CW incident light, there was strong scattered light only in the input port of the plasmonic waveguide connected with a Mach-Zehnder interferometer, which indicates that the logic signal '1' is inputted into the plasmonic
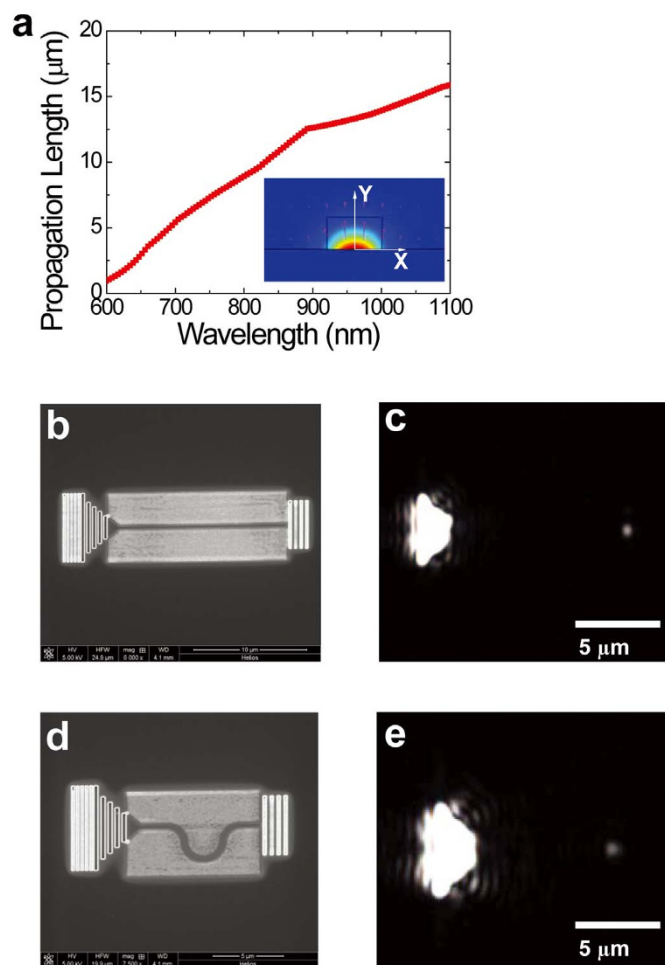
Figure 4 | Characteristics of the plasmonic waveguide. (a) Calculated propagation length for the single SPP waveguide mode. Insert shows the single SPP mode at the cross section, The red arrows indicate the polarization direction. (b) Top-view SEM image for the 15-μm straight plasmonic waveguide. (c) Measured CCD image of the 15-μm straight plasmonic waveguide under excitation of a CW laser with a of wavelength 850 nm. (d) Top-view SEM image of an 11.7-μm bend plasmonic waveguide. (e) Measured CCD image of the 11.7-μm bend plasmonic waveguide under excitation of a CW laser with a of wavelength 850 nm.

waveguide connected with a Mach-Zehnder interferometer, while the logic signal '0' is inputted in the straight plasmonic waveguide. No scattered light was obtained from the decoupling grating in output port, as shown in Fig. 5g, which corresponds to the output logic '0'. This implies that the logic signal propagated in the straight plasmonic waveguide is less than that in the plasmonic waveguide connected with a Mach-Zehnder interferometer. The same case was obtained when the logic comparison sample was excited by a CW incident light with a wavelength of 800 nm (Fig. 5h), 900 nm (Fig. 5i), and 1000 nm (Fig. 5k). The measured results are in agreement with the calculated ones by using the finite element method shown in Fig. S2 in the Supplementary Information. This confirms that the logic comparison sample performs excellently in a large wavelength of 300 nm. The propagation losses in the bended plasmonic waveguide ensure that an output logic '0' can be obtained in a broad wavelength range, greatly contributing to the perfect performance of the logic comparison device. Therefore, the obstacle of inherent Ohmic losses of metal is overcome. The scattered light intensity was obtained from the measured CCD image. The intensity contrast ratio between the output logic '1' and '0' can be calculated from $10 \cdot \log(P_1/P_0)$, where P_1 and P_0 are the

signal intensity of logic '1' and '0', respectively[27]. The measured intensity contrast ratio between the output logic '1' and '0' is shown in Fig. 5l. It is obvious that a high average intensity contrast ratio of over 12 dB can be obtained.

Dual-bit all-optical logic comparator. Figure 6a illustrates the function of all-optical logic comparator for the dual-bit logic signals. When the incident logic signals '11' is inputted in the port '+' while '01' in the port '-', an output logic of '1' is obtained, which implies that the logic signal in the port '+' is larger than that in the port '-'. When the incident logic signals '01' is inputted in the port '+' while '11' in the port '-', an output logic of '0' is obtained, which implies that the logic signal in the port '+' is smaller than that in the port '-'. The SEM image of the logic comparator samples performing the logic operating of dual-bit logic signal comparison is shown in Fig. 6b and d, which are composed of two straight plasmonic waveguides and three plasmonic waveguides connected with a Mach-Zehnder interferometer. There were four input ports, ports A and B for the higher-bit comparison, while ports C and D for the lower-bit comparison. The dimensions of the layout of dual-bit logic comparator for each part were illustrated in Fig. 6(b). In the plasmonic waveguide A, the length between the point of juncture and the end of the waveguide was 15.17 μm. In the plasmonic waveguide B, the horizontal distance between the input port and the point of juncture was 10.17 μm, and the radius of the bended waveguide was 1.7 μm. In the plasmonic waveguide C, the length of the straight waveguide was 10.17 μm, and the radius of the bended waveguide was 4.8 μm. In the plasmonic waveguide D, the horizontal distance between the input port and the point of juncture was 10.17 μm, and the radius of the bended waveguide was 1.7 μm. The basic principle of the design is to use a plasmonic waveguide as short as possible to realize the dual-bit logic comparison function. To perform the logic operation of comparison between logic signals '11' and '01', we etched a SPP light source connected with a triangular access waveguide only in the input ports of the plasmonic waveguide A, C, and D, as shown in Fig. 6b. AC for one input dual-bit logic signal, while BD for the other input dual-bit logic signal. Under excitation of a 1000-nm CW incident light, there was strong scattered light only in the input port of the plasamonic waveguide A, C, and D, which indicates that the logic signal '1' is inputted into the plasmonic waveguide A, C, and D, while the logic signal '0' is inputted in the plasmonic waveguide B. Distinct scattered light was obtained from the decoupling grating in output port, as shown in Fig. 6c, which corresponds to the output logic state '1'. The relatively weak logic state of "1" shown in Fig. 6(c) originates from large SPP propagation losses in an over 25-μm-long PVA-loaded plasmonic waveguide. This implies that the dual-bit logic signal formed by logic states propagating in the plasmonic waveguides A and C (i.e., logic signal '11') is larger than that formed by logic states propagating in the plasmonic waveguides B and D (i.e., logic signal '01'). To perform the logic operation of comparison between logic signals '01' and '11', we etched a SPP light source connected with a triangular access waveguide only in the input ports of the plasmonic waveguide B, C, and D, as shown in Fig. 6d. AC for one input dual-bit logic signal, while BD for the other input dual-bit logic signal. Under excitation of a 1000-nm CW incident light, there was strong scattered light only in the input port of the plasmonic waveguide B, C, and D, which indicates that the logic signal '1' is inputted into the plasmonic waveguide B, C, and D, while the logic signal '0' is inputted in the plasmonic waveguide A. No scattered light was obtained from the decoupling grating in output port, as shown in Fig. 6e, which corresponds to the output logic '0'. This implies that the dual-bit logic signal formed by logic states propagating in the plasmonic waveguides A and C (i.e., logic signal '01') is less than that formed by logic states propagating in the plasmonic waveguides B and D (i.e., logic signal '11'). The propagation losses in the bended plasmonic waveguide also
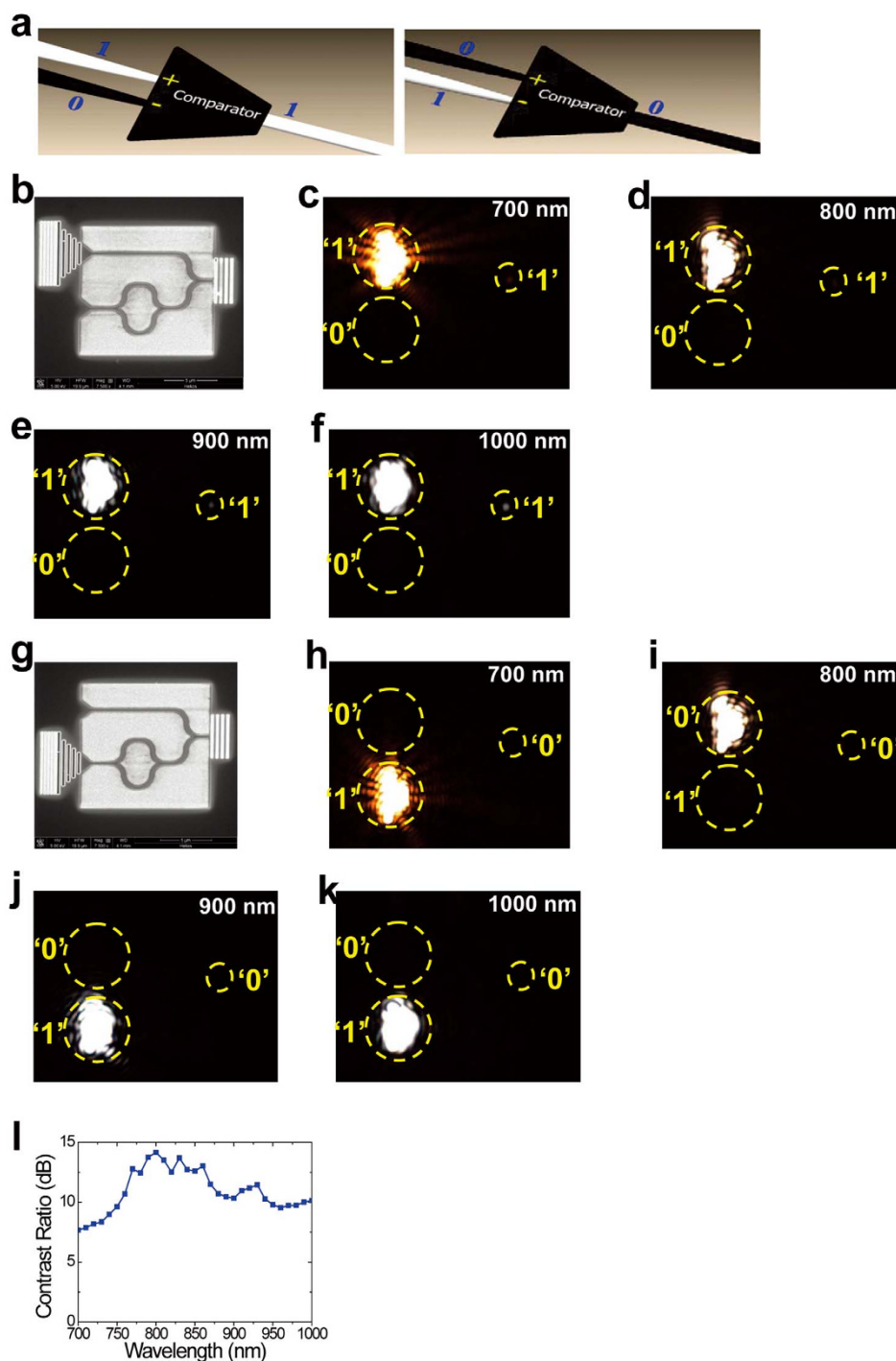
Figure 5 | Performances of all-optical plasmonic logic comparator for single-bit logic signal comparision. (a) Schematic diagram of all-optical plasmonic logic comparator model. (b) Top-view SEM image of the comparator sample with the operation of comparing logic signals '1' and '0'. Measured CCD images of the logic comparator sample with the operation of comparing logic signals '1' and '0' under excitation of a CW incident laser with a wavelength of 700 nm (c), 800 nm (d), 900 nm (e), and 1000 nm (f). (g) Top-view SEM image of the comparator sample with the operation of comparing logic signals '0' and '1'. Measured CCD images of the logic comparator sample with the operation of comparing logic signals '0' and '1' under excitation of a CW incident laser with a wavelength of 700 nm (h), 800 nm (i), 900 nm (j), and 1000 nm (k). (l) Measured intensity contrast ratio between the output logic '1' and '0' as a function of incident laser wavelength.

contribute to the perfect performance of the logic comparison device. To further confirm the function of the dual-bit all-optical logic comparators, we calculated the power flow distributions in the plane 100 nm above the Au surface, and the calculated results are shown in Fig. 6f and g. The experimental results are in good agreement with the results of the 3D numerical simulation.

Discussion

In our experiment, the logic comparison function is realized based on the high digit priority principle, i.e. the high digit determines the output logic state. For two incident dual-bit logic signals, the high digits are compared preferentially. If two high digits are not equal, the lower bits do not need to be compared, and the comparison results
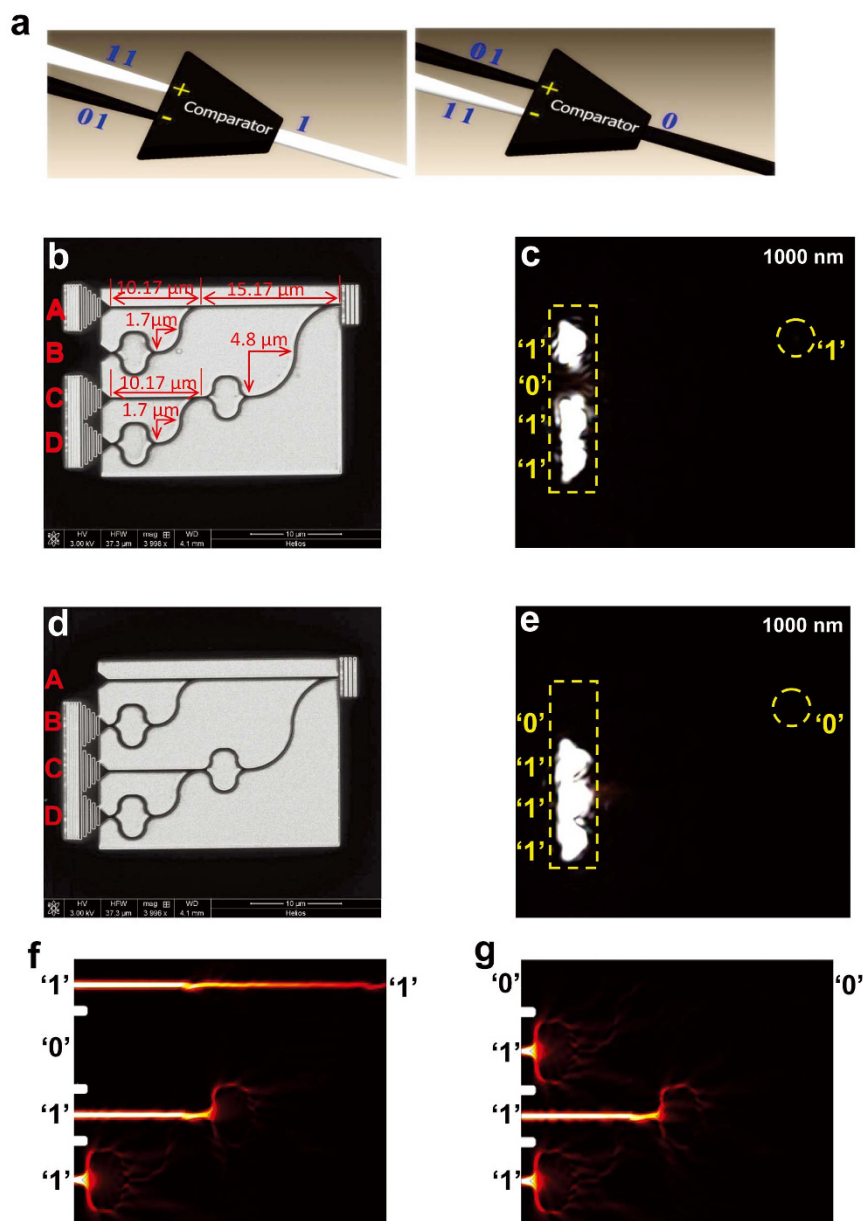
Figure 6 | Performances of all-optical plasmonic logic comparator for dual-bit logic signal comparison. (a) Schematic diagram of all-optical plasmonic logic comparator model. (b) The top-view SEM images of the all-optical plasmonic logic comparator with the operation of comparing logic signals '11' and '01'. (c) Measured CCD image of the logic comparator sample under excitation of a CW laser with a wavelength of 1000 nm. (d) The top-view SEM images of the all-optical plasmonic logic comparators with the operation of comparing logic signals '01' and '11'. (e) Measured CCD image of the logic comparator sample under excitation of a CW laser with a wavelength of 1000 nm. (f) 3D numerical simulation result for the power flow distribution of the plane 100 nm above the Au surface for logic comparator shown in (b). (g) 3D numerical simulation result for the power flow distribution of the plane 100 nm above the Au surface for logic comparator shown in (d) under excitation of a CW laser with a wavelength of 1000 nm.

are determined directly by the high bits. However, if the high bit is equal, the lower bit comparison is necessary to determine which logic signal is "larger". The lower bit comparison is converted to a single-bit comparison, which is also the simplest logic comparison case. There are distinctive advantages for the approach we used to realize chip-integrated ultrawide-band all-optical logic comparator. Firstly, though ultrawide-band unidirectional SPP light source is integrated with the logic comparator device in the same plasmonic chip, ultra-compact device size is maintained. The device size is less than 10 μm for the single-bit logic comparator, and less than 20 μm for the dual-bit logic comparator. Secondly, the obstacles of inherent Ohmic losses of metal and limited propagation length of SPPs are circum-vented by using a unique polymer-loaded plasmonic waveguide

structure and device configuration. Thirdly, the logic comparator device is realized directly in plasmonic circuits, which ensures high-density on-chip integration applications. Fourthly, no any high-power requirement is needed. Moveover, the operation band range can be extended easily to infrared range by adjusting the structure parameters. As our logic comparators are linear passive nano-devices instead of nonlinear devices, our devices response immediately and do not have any delay time. Limited by the measurement systems, the response time is expected to be shorter than several femtoseconds order. Accordingly, the speed of these optical logic comparators is better than 1000 TB/s.

In conclusion, we realized a nanoscale all-optical logic comparator suitable for on-chip integration applications in plasmonic circuits.

The ultrabroad operating wavelength range from 700 to 1000 nm, ultrahigh output logic state contrast ratio of more than 25 dB, and the excellent dual-bit comparison function were achieved. No high power requirement is needed. Moreover, nanoscale SPP light source is integrated with the logic comparator device on the same chip. This work not only paves a way for the realization of complex logic device such as adders and multiplier, but also opens up the possibility for realizing quantum solid chips based on plasmonic circuits.

Methods

Numerical simulation. Numerical simulations were performed by using the commercial finite element (FEM) solver of COMSOL Multiphysics. The refractive index of the dielectric film was 1.50, and the permittivity of the gold was calculated as a function of the wavelength using interpolation and was taken from Ref. 21. Here, the two-dimensional Mode analysis module and the three-dimensional Frequency domain module were used. The transmittance of the plasmonic crystal energy band was defined the quotient between the output power flow of the Au-PVA configuration with plasmonic crystal and that without plasmonic crystal. The output of the plasmonic waveguide was performed using three-dimensional model with the single SPP mode input.

Sample fabrication. The gold film was fabricated using a laser molecular beam epitaxy (LMBE) growth system (Model LMBE 450, SKY Company, China). The beam (wavelength 248 nm, a pulse repetition rate 5 Hz) output from an excimer laser system (Model COMPexPro 205, Coherent Company, USA) was used as the light source. The beam is focused onto a gold target mounted on a rotating holder, 15 mm away from the silicon dioxide substrate. A typical energy density of the excitation laser is about 500 mJ/cm^2. The growth rate measured by a film thickness/rate monitor is about 0.01 nm/pulse. PVA powder with an average molecular weight of 30,000 (J&K company, China) is dissolved in de-ionized water with a weight ratio of 1 : 16. The spin coating method is used to fabricate the PVA layer on the surface of the gold films. A FIB etching system (Model Helios NanoLab 600, FEI Company, USA) is employed to prepare the patterns of the nanoslit and the 1D plasmonic crystal. The spot current of the ion beam was only 24 pA to improve the etching quality.

Micro-spectroscopy measurement setup. In our experiment, a micro-spectroscopy measurement system is used to measure the plasmonic all-optical logic comparator samples. The nanoslits are normally illuminated from the back side using a p-polarized CW Ti:sapphire laser (Model Mira 900F, Coherent Company, USA) with different wavelengths. The optical-thick gold film can prohibit the direct transmission of the incident laser beam. The line width of the laser spectrum curve is about 1.5 nm which ensures that only the specified quasi-monochromatic SPP modes can be excited by the nanoslit. The SPP mode is scattered using decoupling grating in the output port. The scattered light is collected by a long working distance objective (Mitutoyo 20, NA = 0.58) and then imaged onto a charge coupled device (CCD).

1. Joannopoulos, J. D., Johnson, S. J., Winn, J. N. & Meade, R. D. *Photonic crystals: Molding the Flow of Light* (Princeton University press, Princeton, 2008).
2. Jalali, B. & Fathpour, S. Silicon photonics. *J. Lightwave Technol.* **24**, 4600–4615 (2006).
3. Barnes, W. L., Dereux, A. & Ebbesen, T. W. Surface plasmon subwavelength optics. *Nature* **424**, 824–830 (2003).
4. Zia, R., Schuller, J. A., Chandran, A. & Brongersma, M. L. Plasmonics: the next chip-scale technology. *Mater. Today* **9**, 20–27 (2006).
5. Ebbesen, T. W., Genet, C. & Bozhevolnyi, S. I. Surface-plasmon circuitry. *Phys. Today* **61**, 44–50 (2008).
6. Ozbay, E. Plasmonics: merging photonics and electronics at nanoscale dimensions. *Science* **311**, 189–193 (2006).
7. Wei, H. *et al*. Quantum dot-based local field imaging reveals plasmon-based interferometric logic in silver nanowire networks. *Nano Lett.* **11**, 471–475 (2011).
8. Wei, H., Wang, Z. X., Tian, X. R., Kall, M. & Xu, H. X. Cascaded logic gates in nanophotonic plasmon networks. *Nature Commun.* **2**, 387 (2011).
9. Fu, Y. L. *et al*. All-optical logic gates based on nanoscale plasmonic slot waveguides. *Nano Lett.* **12**, 5784–5790 (2012).
10. Lu, C. C. *et al*. Ferroelectric hybrid plasmonic waveguide for all-optical logic gate applications. *Plasmonics* **8**, 749–754 (2013).
11. Lu, C. C., Hu, X. Y., Yang, H. & Gong, Q. H. Integrated all-optical logic discriminators based on plasmonic bandgap engineering. *Sci. Rep.* **3**, 2778; doi:10.1038/srep02778 (2013).
12. Garai, S. K. A method of developing frequency encoded multi-bit optical data comparator using semiconductor optical amplifier. *Opt. Laser Technol.* **43**, 124–131 (2011).
13. Wang, Y., Zhang, X. L., Dong, J. J. & Huang, D. X. Simultaneous demonstration on all-optical digital encoder and comparator at 40 Gb/s with semiconductor optical amplifiers. *Opt. Express* **15**, 15080–15085 (2007).
14. Scaffardi, M., Ghelfi, P., Lazzeri, E., Poti, L. & Bogoni, A. Photonic processing for digital comparison and full addition based on semiconductor optical amplifiers. *IEEE J. Sel. Top. Quantum Electron.* **14**, 826–833 (2008).
15. Kaur, S. All optical data comparator and decoder using SOA-based Mach-Zehnder interferometer. *Optik* **124**, 2650–2653 (2013).
16. Zhang, Y., Lei, L., Dong, J. J. & Zhang, X. L. Simultaneous all-optical digital comparator and dual-directional half-subtractor for two-input 40 Gbit/s DPSK signals employing SOAs. *Opt. Commun.* **285**, 407–411 (2012).
17. Mukherjee, K. & Ghosh, P. Alternative method of implementation of frequency encoded N bit comparator exploiting four wave mixing in semiconductor optical amplifiers. *Optik* **123**, 2276–2280 (2012).
18. Lu, C. C., Hu, X. Y., Yang, H. & Gong, Q. H. All-optical logic binary encoder based on asymmetric plasmonic nanogrooves. *Appl. Phys. Lett.* **103**, 121107 (2013).
19. Bozhevolnyi, S. I., Volkov, V. S., Devaux, E., Laluet, J. Y. & Ebbesen, T. W. Channel plasmon subwavelength waveguide components including interferometers and ring resonators. *Nature* **440**, 508–511 (2006).
20. Krasavin, A. V. & Zayats, A. V. Three-dimensional numerical modeling of photonic integration with dielectric-loaded SPP waveguides. *Phys. Rev. B* **78**, 045425 (2008).
21. Johnson, P. B. & Christy, R. W. Optical constants of the noble metals. *Phys. Rev. B* **6**, 4370–4379 (1972).
22. Chen, J. J., Li, Z., Yue, S. & Gong, Q. H. Highly efficient all-optical control of surface-plasmon-polariton generation based on a compact asymmetric single slit. *Nano Lett.* **11**, 2933–2937 (2011).
23. Barnes, W. L., Preist, T. W., Kitson, S. C. & Sambles, J. R. Physical origin of photonic energy gaps in the propagation of surface plasmons on gratings. *Phys. Rev. B* **54**, 6227–6244 (1996).
24. Tejeira, F. L. *et al*. Efficient unidirectional nanoslit couplers for surface plasmons. *Nature Phys.* **3**, 324–328 (2007).
25. Chen, J. J., Li, Z., Yue, S. & Gong, Q. H. Efficient unidirectional generation of surface plasmon polaritons with asymmetric single-nanoslit. *Appl. Phys. Lett.* **97**, 041113 (2010).
26. Lu, C. C., Hu, X. Y., Yang, H. & Gong, Q. H. Ultrawide-Band Unidirectional Surface Plasmon Polariton Launchers. *Adv. Optical Mater.* **1**, 792–797 (2013).
27. Zhang, Y. L., Zhang, Y. & Li, B. J. Optical switches and logic gates based on self-collimated beams in two-dimensional photonic crystals. *Opt. Express* **15**, 9287–9292 (2007).

Acknowledgments

Author contributions

C.L. and X.H. proposed the idea. C.L., X.H. and H.Y. performed measurements. C.L., X.H., H.Y. and Q.G. analyzed data and co-wrote the manuscript.

Additional information